THE JOURNAL OF PHYSICAL CHEMISTRY C

Article

Cite This: J. Phys. Chem. C 2018, 122, 2712−2716

pubs.acs.org/JPCC

Oxygen Reduction Reaction on Classically Immiscible Bimetallics: A Case Study of RhAu

Hao Li,[†,‡] Long Luo,[†,§] Pranaw Kunal,[†] Cecile S. Bonifacio,[∥] Zhiyao Duan,[†,‡] Judith C. Yang,*[,∥] Simon M. Humphrey,*[,†] Richard M. Crooks,*[,†,§] and Graeme Henkelman*[,†,‡]

[†]Department of Chemistry, [‡]Institute for Computational and Engineering Sciences, and [§]Texas Materials Institute, The University of Texas at Austin, 105 E. 24th Street, Stop A5300 Austin, Texas 78712, United States

[∥]Department of Chemical and Petroleum Engineering and Department of Physics, University of Pittsburgh, Pittsburgh, Pennsylvania 15261, United States

Supporting Information

ABSTRACT: The catalytic properties of bulk-immiscible alloys are less explored than their bulk-miscible counterparts due to inherent difficulties in their synthesis and stabilization. The development of alternative synthetic methods can, however, provide routes toward bulk-immiscible nanoparticles with metastable randomly alloyed structures. In this study, we combine computational screening and a microwave-based synthesis method to target bulk-immiscible alloys that show enhanced reactivity over pure metals for the oxygen reduction reaction (ORR). A number of systems are identified theoretically as promising ORR catalysts. The theoretical predictions are experimentally verified for the RhAu system, for which a specific surface ensemble is identified as being highly active in the ORR.

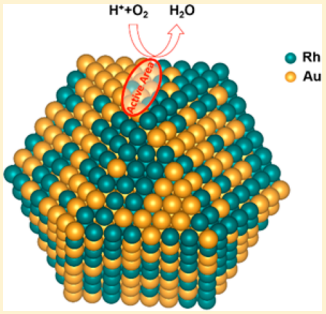

INTRODUCTION

The proton exchange membrane fuel cell (PEMFC) is an electrochemical device that produces electrical energy directly from hydrogen fuels. PEMFCs are key components of the hydrogen economy, with clear applications in the transportation sector. Significant problems that limit the widespread use of PEMFCs are the high cost of Pt as the working cathode, and energy losses caused by the high overpotential required to achieve the oxygen reduction reaction (ORR). In order to improve further PEMFC efficiency, better ORR catalysts must be identified; from an economical perspective, less reliance upon Pt is also desirable.

Pt is the most effective monometallic catalyst for the ORR. Theoretical volcano plots show that Pt binds oxygen-containing intermediates in the ORR (OH, O, OOH) *ca.* 0.1 eV stronger than optimal; slightly weaker oxygen adsorption on the surface is understood to enhance the ORR activity.[1] Subsurface alloying has been shown to fine-tune the position of the *d*-band center of a Pt monolayer skin via both ligand and lattice strain effects, and is thus a promising approach to design better Pt alloy catalysts for the ORR.[2] Consistent with these theoretical calculations, a number of Pt-skin catalysts have already been demonstrated to possess enhanced reactivity for the ORR.[2−10]

Nanoparticle catalysts synthesized with thin Pt shells ("Pt-skin NPs") are potentially ideal for the ORR. Synthetic control over the skin thickness permits fine-tuning of substrate binding energies (*ca.* 0.1 eV) via ligand (or electronic) effects exerted between the Pt-skin and subsurface metal atoms. In turn, this allows for optimization of ORR reactivity. In contrast, ensemble effects are more important than ligand and strain effects in bi-/multimetallic alloys since they more significantly determine the surface binding energies of chemical intermediates,[11−16] primarily based on the average properties of the host metals present at the surface. Hence, mixing two metals whose binding energies for intermediates lie on either side of Pt could provide a near optimal resulting binding energy that is close to that of Pt. This strategy is reliant upon ensuring that particular bimetallic ensembles are present on the catalyst surface. By use of the ensemble effect to achieve better reactivity, nanoparticle alloys have been demonstrated for a plethora of other reactions,[11−13] yet the ensemble effect is much less studied for the ORR.[17]

According to the volcano-like ORR activity plot derived for monometallic surfaces developed by Nørskov et al.,[1] Au and Ag bind oxygen too weakly for the ORR, while most earlier transition metals (e.g., Ni, Cu, Rh, Pd, and Ir) bind both oxygen and hydroxyl too strongly. Consequently, Au- and Ag-based alloys were chosen for our investigation of the ensemble effect. It should be noted that all Au- and Ag-based alloys considered here are immiscible in the bulk (Figure S1), with the exception of PdAg, CuAu, and PdAu. Fortunately, even for classically immiscible alloys, interface sites (e.g., X_1Y_2 and X_2Y_1) between segregated (or partially segregated) phases could still have high catalytic activities.

Received: November 6, 2017
Revised: December 19, 2017
Published: January 11, 2018

DOI: 10.1021/acs.jpcc.7b10974
J. Phys. Chem. C 2018, 122, 2712−2716

In this study, we carried out a computational screening of Au- and Ag-based alloys in the ORR. One of the most promising candidates predicted by this study was the RhAu alloy. Nanoparticles (NPs) of this alloy were synthesized using a microwave-assisted solution-phase technique, permitting structural characterization and electrochemical testing. For this system, we are able to show that the theoretical predictions were verified experimentally regarding the most active ensemble site for the ORR.

RESULTS AND DISCUSSION

Density functional theory (DFT) is a proven computational tool that can be used to design and understand nanoalloy catalysts.[2,11,18] To screen for alloy catalysts, the oxygen and hydroxyl binding energies were calculated at different triatomic ensembles on Au- and Ag-based surface alloys to determine their theoretical overpotential for the ORR. Oxygen favors the 3-fold hollow site on (111) noble metal surfaces that display face-centered cubic (FCC) packing; therefore, triatomic ensembles are the smallest unit that need to be considered. For each surface alloy, four triatomic ensembles were considered: Y_3, X_1Y_2, X_2Y_1, and X_3 with X = Pd, Pt, Cu, Rh, Ni, and Ir and Y = Au and Ag. Using the example of a Au(111) surface alloyed with metal X, the possible triatomic ensembles are shown in the inset of Figure 1. The calculated oxygen and hydroxyl energies are plotted on the ORR volcano activity plot reproduced from ref 1. According to the results shown in Figure 1 (with additional details in Figure S2), several Au- and Ag-based alloys have triatomic ensembles with promising ORR activities. More details about the computational methods used can be found in the Supporting Information. Previous experimental studies have shown promising ORR activities by other bimetallic systems including PdAu,[19] PtAu[20] and PdAg (under alkaline conditions),[17] but other previously unidentified candidate systems still remain, including the RhAu alloy featured in this work.

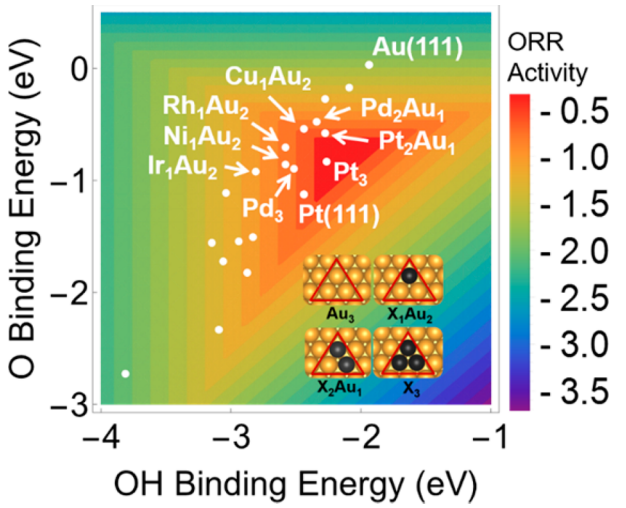

Figure 1. Volcano activity plot predicts ORR activities at different triatomic ensembles on Au(111). The inset shows the triatomic ensembles on Au(111) surfaces formed by alloying with a second metal. Gold spheres represent Au atoms; black spheres represent the alloy element X (X = Pd, Pt, Cu, Rh, Ni, and Ir). The ensemble geometries on Au-based surface alloys are in accordance with the inset. Details of the calculated volcano plot are given in the Supporting Information. Comparable results for Au- and Ag-based triatomic ensembles can be found in Figures S2 and S3.

The activities of different RhAu ensembles are shown in Figure 2. Rh_1Au_2 was predicted to be the most active site for ORR since the addition of Au effectively weakens the binding energies of O and OH on Rh. The binding energy of O was found to be linearly correlated with the number of Au atoms at the 3-fold hollow site. Conversely, the binding energy of OH appears to be less effectively tuned with increasing Au content in the ensemble. The reason is that adsorbed OH was found to bind to the Rh atoms in the ensemble and not to Au atoms. The OH binding energy is only tuned as a result of the electronic effect between Rh and Au. The weaker OH binding at Au-rich ensembles is governed by the downshift of the *d*-band center of the binding site (Figure S4). The binding energies of O and OH can even be tuned in opposite directions, as in the case of PtAg (Figure S3h). Although not beneficial for optimizing the ORR, this relative tuning for different intermediates could be useful for controlling reaction selectivity, in which the differentiation of binding energies of competing intermediates is an important factor. It should be noted that at lower potentials in the ORR experiments, the surface coverage of adsorbates (e.g., O, OH, and OOH) are expected to decrease, but we do not expect coverage effects to change the qualitative conclusions drawn in this study.

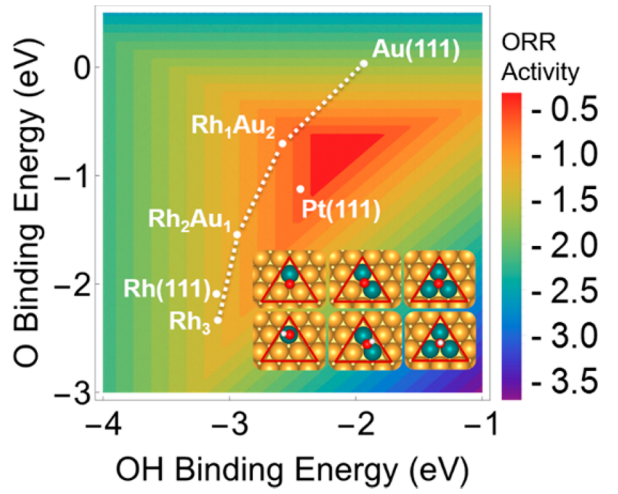

Figure 2. Oxygen and hydroxyl binding energies calculated at the Rh-triatomic ensembles on Au(111). The inset shows the optimal binding configurations of oxygen and hydroxyl at different triatomic ensembles. The gold, teal, red, and white spheres represent Au, Rh, O, and H atoms, respectively.

We have taken a further step to test if the Rh_1Au_2 ensemble remains the most active site over a range of overall alloy compositions. In our test, the average oxygen binding energies were calculated at four triatomic ensembles on slab models of RhAu alloys with different relative compositions: $Rh_{25}Au_{75}$, $Rh_{50}Au_{50}$, and $Rh_{75}Au_{25}$ (Figure S5). These calculations indicate that the oxygen binding energies are only slightly influenced by the overall composition of the alloy and the Rh_1Au_2 ensemble remains the most active site regardless of alloy composition.

Chemical synthesis of RhAu alloys is difficult because Rh and Au are immiscible in the bulk, undergoing complete segregation from the hot (2158 K) comelt. A previous theoretical study suggested that phase separation could be reduced in small

DOI: 10.1021/acs.jpcc.7b10974
J. Phys. Chem. C 2018, 122, 2712−2716

nanoparticles (NPs) by exploiting size-confinement effects to obtain "trapped" metastable alloys.[21] Recently, our theoretical and experimental studies have shown that, in addition to miscible bimetallics (e.g., PdAu[13]), more unusual classically immiscible alloy NPs (e.g., RhPd, RhAg, and RhAu)[12,15,22] can be synthesized as metastable solid solutions on the nanoscale. RhAu NPs with desired Rh:Au compositions can be prepared via solution-phase coreduction of molecular Rh(III) and Au(III) precursors under microwave irradiation (μwI), in the presence of poly(vinylpyrrolidone) (PVP).[12] When supported on silica, the RhAu NP catalysts out-perform their monometallic counterparts in the vapor-phase hydrogenation of alkenes. The nonequilibrium heating mechanism of dipolar coupling between μwI and polar species that induces so-called "hot-spot" generation is thought to play a key role in accessing kinetically stable nanostructures. Additionally, while some classically immiscible alloy NPs can undergo gradual segregation and/or adsorbate-induced restructuring, the presence of active bimetallic ensembles at the interface between the constituents may still provide highly catalytically active sites.[12]

Various compositions of RhAu alloy NPs were synthesized under μwI using a simplified version of the original method.[12] Instead of two subsequent injections of Rh(III) and Au(III) precursors at different rates, a single injection of premixed metal precursors into a hot ethylene glycol/PVP mixture was used. The injection rate of the metal precursors was optimized for each reaction to yield similar sized Rh_xAu_{100-x} NPs. The average diameter of the resulting Rh_xAu_{100-x} alloy NPs of various compositions was between 3−4 nm. Specifically, the lowest average diameter of 3.4 nm (σ = 0.8 nm) was observed for $Rh_{91}Au_{09}$ NPs; the highest average diameter of 4.2 nm (σ = 1.8 nm) for $Rh_{50}Au_{50}$ NPs was determined by transmission electron microscopy (TEM; size histograms for the NPs are shown in Figures S6 and S7). Powder X-ray diffraction (PXRD) analysis of the RhAu alloy NPs showed a clear shift in the lattice constant in response to changing Rh:Au composition. The data exhibited slight deviations from Vegard's law, consistently favoring larger lattice parameters than expected, which may be indicative of some overincorporation of Au vs the nominal (target) compositions (Figures S8 and S9). 2-D scanning TEM in energy-dispersive spectroscopy (EDS) mode gave elemental maps of individual NPs that confirms coincorporation of both Rh and Au, and indicates some degree of Rh surface segregation (*vide infra*; Figure S10).

The as-synthesized RhAu NP catalysts were thermally annealed at 185 °C to remove the PVP capping agent before ORR activity tests.[23] There are several notable aspects of the analytical data following heating. First, X-ray photoelectron spectroscopy (XPS) spectra showed an average N signal reduction of 65% after the thermal treatment (Figure S11 and Table S1), which indicates partial removal of PVP. At the same time, Rh in the NPs was found to be partially oxidized to Rh(III) as indicated by the emergence of a new peak in the XPS spectrum at a binding energy of 308.2 eV (Figure S11).[24] Second, the thermally treated RhAu NPs exhibited similar sizes as the as-synthesized NPs (see Figures S6 and S7). Third, isothermal heating led to a qualitative increase in surface segregation of Rh. For example, the TEM-EDS data for an annealed $Rh_{50}Au_{50}$ NP shows the appearance of 1−2 nm Rh-rich clusters on the surface of the NPs (Figure S10). In essence, the extent of segregation can be considered to produce "leopard spot" bimetallics. The partially segregated NPs resist further (complete) segregation, suggesting that the leopard spot structures become metastable with respect to further segregation. Pure Rh and Au NPs or NPs with hemispheres of each metal were not observed, in agreement with the PXRD characterization of the annealed nanoparticle samples (Figure S8). A similar segregation of Rh was found in the absence of atmospheric O_2 when the heating was performed within the TEM (Figure S12). These combined observations are in agreement with the oxidation potentials of Au(0) vs Rh(0), which would suggest that surface segregation of Rh is driven by its comparative ease of oxidation to Rh(I) and Rh(III). Fourthly, as will be discussed next, the ORR activities of RhAu NPs were significantly improved after a mild-temperature heating (Figure S13).

The ORR activities of thermally annealed RhAu NPs were determined using rotating disk voltammetry (RDV). A catalyst-modified glassy carbon rotating disk electrode (GC-RDE) was prepared by adding DI water to the thermally annealed RhAu NPs to prepare a catalyst ink, and then dropcasting 6 μL of this ink onto the GC-RDE. The ink was dried under mild N_2 flow prior to electrochemical tests. The catalyst-modified GC-RDE was scanned from 1.0 to 0.0 V vs RHE in O_2-saturated 0.1 M $HClO_4$ for three consecutive cycles. The polarization curves shifted positive by ∼100−300 mV during the first two scans and remained unchanged after the second scan (Figure S14). This initial shift was possibly due to the electroreduction of Rh(III) species formed during the thermal removal of PVP, which creates more active RhAu surface ensembles for the ORR.[25] The ORR polarization curves of RhAu NPs, pure Rh and Au NPs at the second scan are given in Figure 3a. The onset potentials for the ORR, defined as the potential where the current reaches 0.1 mA/cm^2, by RhAu alloy NPs are similar ∼0.817 V vs. RHE. In contrast, the onset potentials for pure Rh and Au NPs occurred at *ca.* 0.50 V vs RHE, which is 300 mV more negative than for RhAu alloy NPs. This observation suggests that the surface of the RhAu NPs has the same highly active bimetallic sites regardless of their compositions (though, of course, the number density of such sites varies depends on the overall stoichiometry). According to the calculations discussed earlier, these are Rh_1Au_2 atomic ensembles. Despite similar onset potentials, the RhAu alloy NPs exhibit composition-dependent ORR rates following the trend: $Rh_{33}Au_{67}$ > $Rh_{50}Au_{50}$ > $Rh_{67}Au_{33}$ > $Rh_{90}Au_{10}$. However, because of the heat-induced Rh segregation discussed earlier, and variations in the percentage of PVP removed during heating, it is difficult to draw specific conclusions about how the surface composition affects the ORR. However, together with the observation that the Rh−Au interface remains after thermal treatment (Figures S10 and S12), the general trend shown in Figure 3a clearly indicates that Au sites play an important role for the ORR and the stability of the NPs is not a critical issue for ORR catalysis.

Thus far, we have only considered ORR activities of RhAu NPs in terms of their onset potentials and current densities obtained from RDVs. To gain further insight into the ORR reaction pathways at the surfaces of RhAu NPs, we carried out rotating ring-disk voltammetry (RRDV). Figure 3b shows the current densities at the disk electrode (i_D, top frame) and the corresponding ring currents (i_R, middle frame) as well as the number of electrons (N_e) involved in the ORR (bottom frame). N_e was calculated from i_D and i_R using Eqn. 1.[26] The ring collection efficiency was experimentally determined to be 0.37.

$$N_e = 4 - (2 \times i_R)/(0.37 \times i_D) \quad (1)$$

DOI: 10.1021/acs.jpcc.7b10974
J. Phys. Chem. C 2018, 122, 2712−2716

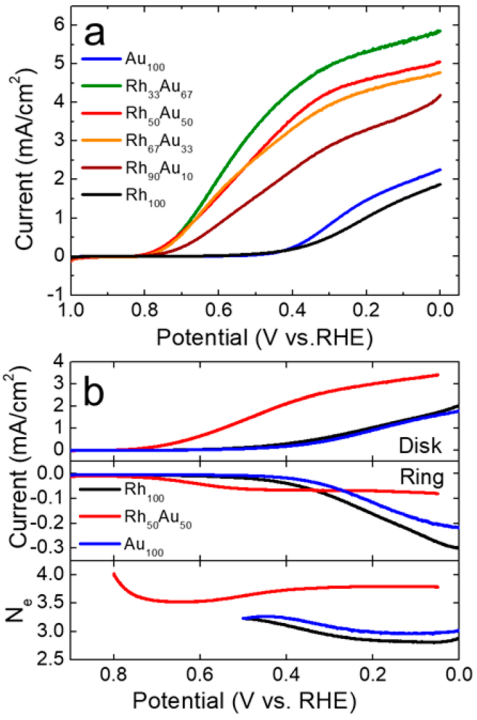

Figure 3. (a) ORR polarization curves for GC-RDEs modified with thermally annealed Rh_xAu_{100-x} NPs (x = 0, 33, 50, 67, 90, and 100). The electrolyte solution was O_2-saturated 0.10 M $HClO_4$, and the scan rate was 5.0 mV/s. (b) RRDV of Rh_{100}, $Rh_{50}Au_{50}$, and Au_{100} modified glassy carbon electrodes. Key: top frame, disk currents arising from ORR; middle frame, ring current from the oxidation of hydrogen peroxide generated at the disk electrode during the ORR; bottom frame, the apparent number of electrons (N_e) calculated from the disk and ring currents. The potential of the Pt ring electrode was held at 0.50 V; the other experimental settings are identical to those in part a.

The $Rh_{50}Au_{50}$ NPs exhibit a higher i_D than either Rh_{100} and Au_{100} at the same potential, whereas i_R for $Rh_{50}Au_{50}$ is lower over most of the potential range examined. In this experiment, i_R corresponds to generation of H_2O_2, which is an undesirable side product of the ORR. Taken together, the higher value of i_D and the lower value of i_R for the $Rh_{50}Au_{50}$ NPs indicates that this material is more selective for formation of water than the pure metals. More quantitatively, in the potential region corresponding to the limiting current, N_e= 3.8, 2.9, and 2.8 for the $Rh_{50}Au_{50}$, Au_{100}, and Rh_{100} NPs, respectively. The increase in N_e observed for $Rh_{50}Au_{50}$ can be attributed to the 4-electron ORR pathway at the RhAu bimetallic ensembles as previously discussed.

To gain a better understanding of the ORR mechanism on RhAu, we calculated the free energy diagram of the reaction for different mechanisms at Rh_1Au_2 triatomic ensembles (Figure 4). The ORR pathway following the O_2 dissociative mechanism is unfavorable as compared to the peroxyl or peroxide pathways because of the high (0.79 eV) barrier for O_2 dissociation. Additionally, the 4-electron reaction should be preferred on the Rh_1Au_2 ensemble since formation of HOOH from OOH is less favorable than the alternative water formation pathway. These predictions are fully consistent with the 4-electron reaction observed experimentally for the RhAu alloys.

CONCLUSIONS

Here, we have shown that RhAu alloy NPs have oxygen and hydroxyl binding energies tuned by the ensemble and electronic

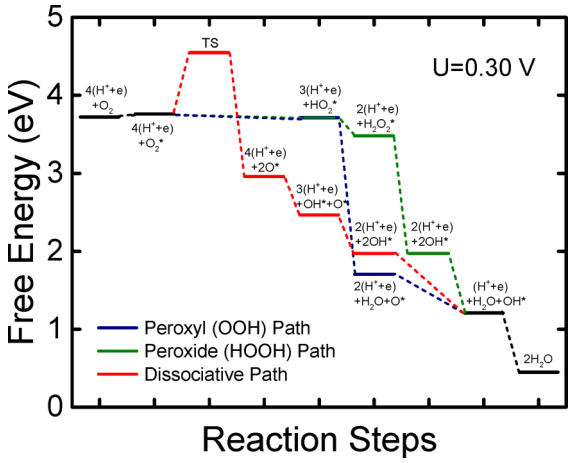

Figure 4. Free energy diagram of 4-electron ORR mechanisms with peroxyl, peroxide and dissociative paths at a Rh_1Au_2 triatomic ensemble on Au(111), at a potential of U = 0.30 V.

effects. The Rh_1Au_2 triatomic ensemble is identified as being active for the ORR. This computational prediction is validated by experimental observations that RhAu alloy NPs have significantly enhanced ORR activities comparing to pure Rh and Au NPs. Being a classically immiscible system, the synthesized RhAu NPs were found to possess some degree of phase segregation before and after heat treatment. Even though the best RhAu alloy NPs in this study do not outperform state-of-art Pt catalysts, the potential catalytic application of nanosized RhAu and other bimetallics that contain elements that are immiscible in bulk phases should not be ignored, because a significant proportion of highly active surface ensembles still prevail.

ASSOCIATED CONTENT

Supporting Information

The Supporting Information is available free of charge on the ACS Publications Web site. The Supporting Information is available free of charge on the ACS Publications website at DOI: 10.1021/acs.jpcc.7b10974.

Additional computational methods and results, synthesis methods, EDS, TEM, XRD, PVP removal, and electrochemistry (PDF)

AUTHOR INFORMATION

Corresponding Authors

*E-mail (J.C.Y.): judyyang@pitt.edu.
*E-mail (S.M.H.): smh@cm.utexas.edu.
*E-mail (R.M.C.): crooks@cm.utexas.edu.
*E-mail (G.H.): henkelman@utexas.edu.

ORCID

Simon M. Humphrey: 0000-0001-5379-4623
Richard M. Crooks: 0000-0001-5186-4878
Graeme Henkelman: 0000-0002-0336-7153

Notes

The authors declare no competing financial interest.

ACKNOWLEDGMENTS

This work was supported by the National Science Foundation under Grant Nos. CHE-1534177 (G.H. and R.M.C.), CHE-1505135 (S.M.H. and G.H.), and CHE-1534630 (J.C.Y.). We

DOI: 10.1021/acs.jpcc.7b10974
J. Phys. Chem. C 2018, 122, 2712−2716

also appreciate support from the Welch Foundation (F-0032, F-1738, and F-1841). C.S.B. and J.C.Y. acknowledge Dr. Marco Cordeiro for technical assistance and the Center for Functional Nanomaterials (CFN) at Brookhaven National Lab supported by the Office of Basic Energy Sciences of the US Department of Energy, Contract No. DE-AC02-05CH11231. Computational resources were provided by the Texas Advanced Computing Center.

REFERENCES

(1) Nørskov, J. K.; Rossmeisl, J.; Logadottir, A.; Lindqvist, L.; Kitchin, J. R.; Bligaard, T.; Jónsson, H. Origin of the Overpotential for Oxygen Reduction at a Fuel-Cell Cathode. *J. Phys. Chem. B* **2004**, *108* (46), 17886−17892.

(2) Zhang, L.; Iyyamperumal, R.; Yancey, D. F.; Crooks, R. M.; Henkelman, G. Design of Pt-Shell Nanoparticles with Alloy Cores for the Oxygen Reduction Reaction. *ACS Nano* **2013**, *7* (10), 9168−9172.

(3) Zhang, J.; Vukmirovic, M. B.; Xu, Y.; Mavrikakis, M.; Adzic, R. R. Controlling the Catalytic Activity of Platinum-Monolayer Electrocatalysts for Oxygen Reduction with Different Substrates. *Angew. Chem., Int. Ed.* **2005**, *44* (14), 2132−2135.

(4) Wang, C.; Chi, M.; Li, D.; Strmcnik, D.; Van Der Vliet, D.; Wang, G.; Komanicky, V.; Chang, K. C.; Paulikas, A. P.; Tripkovic, D.; et al. Design and Synthesis of Bimetallic Electrocatalyst with Multilayered Pt-Skin Surfaces. *J. Am. Chem. Soc.* **2011**, *133* (36), 14396−14403.

(5) Greeley, J.; Stephens, I. E. L.; Bondarenko, a S.; Johansson, T. P.; Hansen, H. a; Jaramillo, T. F.; Rossmeisl, J.; Chorkendorff, I.; Nørskov, J. K. Alloys of Platinum and Early Transition Metals as Oxygen Reduction Electrocatalysts. *Nat. Chem.* **2009**, *1* (7), 552−556.

(6) Adzic, R. R.; Zhang, J.; Sasaki, K.; Vukmirovic, M. B.; Shao, M.; Wang, J. X.; Nilekar, A. U.; Mavrikakis, M.; Valerio, J. A.; Uribe, F. Platinum Monolayer Fuel Cell Electrocatalysts. *Top. Catal.* **2007**, *46* (3−4), 249−262.

(7) Zhang, J.; Mo, Y.; Vukmirovic, M. B.; Klie, R.; Sasaki, K.; Adzic, R. R. Platinum Monolayer Electrocatalysts for O-2 Reduction: Pt Monolayer on Pd(111) and on Carbon-Supported Pd Nanoparticles. *J. Phys. Chem. B* **2004**, *108* (30), 10955−10964.

(8) Stamenkovic, V. R.; Fowler, B.; Mun, B. S.; Wang, G.; Ross, P. N.; Lucas, C. A.; Markovic, N. M. Improved Oxygen Reduction Activity on Pt3Ni (111) via Increased Surface Site Availability. *Science (Washington, DC, U. S.)* **2007**, *315* (5811), 493−497.

(9) Stamenkovic, V. R.; Mun, B. S.; Arenz, M.; Mayrhofer, K. J. J.; Lucas, C. a; Wang, G. F.; Ross, P. N.; Markovic, N. M. Trends in Electrocatalysis on Extended and Nanoscale Pt-Bimetallic Alloy Surfaces. *Nat. Mater.* **2007**, *6* (3), 241−247.

(10) Stamenkovic, V.; Mun, B. S.; Mayrhofer, K. J. J.; Ross, P. N.; Markovic, N. M.; Rossmeisl, J.; Greeley, J.; Nørskov, J. K. Changing the Activity of Electrocatalysts for Oxygen Reduction by Tuning the Surface Electronic Structure. *Angew. Chem., Int. Ed.* **2006**, *45* (18), 2897−2901.

(11) Luo, L.; Duan, Z.; Li, H.; Kim, J.; Henkelman, G.; Crooks, R. M. Tunability of the Adsorbate Binding on Bimetallic Alloy Nanoparticles for the Optimization of Catalytic Hydrogenation. *J. Am. Chem. Soc.* **2017**, *139*, 5538−5546.

(12) García, S.; Zhang, L.; Piburn, G. W.; Henkelman, G.; Humphrey, S. M. Microwave Synthesis of Classically Immiscible Rhodium-Silver and Rhodium-Gold Alloy Nanoparticles: Highly Active Hydrogenation Catalysts. *ACS Nano* **2014**, *8* (11), 11512−11521.

(13) Kunal, P.; Li, H.; Dewing, B. L.; Zhang, L.; Jarvis, K.; Henkelman, G.; Humphrey, S. M. Microwave-Assisted Synthesis of PdxAu100-X Alloy Nanoparticles: A Combined Experimental and Theoretical Assessment of Synthetic and Compositional Effects upon Catalytic Reactivity. *ACS Catal.* **2016**, *6* (8), 4882−4893.

(14) Seraj, S.; Kunal, P.; Li, H.; Henkelman, G.; Humphrey, S. M.; Werth, C. J. PdAu Alloy Nanoparticle Catalysts: Effective Candidates for Nitrite Reduction in Water. *ACS Catal.* **2017**, *7* (5), 3268−3276.

(15) Piburn, G. W.; Li, H.; Kunal, P.; Henkelman, G.; Humphrey, S. M. Rapid Synthesis of RhPd Alloy Nanocatalysts. *ChemCatChem* **2018**, *10*, 329.

(16) Luo, L.; Zhang, L.; Duan, Z.; Lapp, A. S.; Henkelman, G.; Crooks, R. M. Efficient CO Oxidation Using Dendrimer-Encapsulated Pt Nanoparticles Activated with < 2% Cu Surface Atoms. *ACS Nano* **2016**, *10* (9), 8760−8769.

(17) Slanac, D. A.; Hardin, W. G.; Johnston, K. P.; Stevenson, K. J. Atomic Ensemble and Electronic Effects in Ag-Rich AgPd Nanoalloy Catalysts for Oxygen Reduction in Alkaline Media. *J. Am. Chem. Soc.* **2012**, *134* (23), 9812−9819.

(18) Greeley, J.; Nørskov, J. K. Combinatorial Density Functional Theory-Based Screening of Surface Alloys for the Oxygen Reduction Reaction. *J. Phys. Chem. C* **2009**, *113* (12), 4932−4939.

(19) Nie, M.; Shen, P. K.; Wei, Z. Nanocrystaline Tungsten Carbide Supported Au-Pd Electrocatalyst for Oxygen Reduction. *J. Power Sources* **2007**, *167* (1), 69−73.

(20) Hernández-Fernández, P.; Rojas, S.; Ocón, P.; Gómez de la Fuente, J. L.; San Fabián, J.; Sanza, J.; Peña, M. A.; García-García, F. J.; Terreros, P.; Fierro, J. L. G. Influence of the Preparation Route of Bimetallic Pt - Au Nanoparticle Electrocatalysts for the Oxygen Reduction Reaction. *J. Phys. Chem. C* **2007**, *111* (7), 2913−2923.

(21) Christensen, a; Stoltze, P.; Norskov, J. K. Size Dependence of Phase Separation in Small Bimetallic Clusters. *J. Phys.: Condens. Matter* **1995**, *7* (6), 1047−1057.

(22) House, S. D.; Bonifacio, C. S.; Timoshenko, J.; Kunal, P.; Wan, H.; Duan, Z.; Li, H.; Yang, J. C.; Frenkel, A. I.; Humphrey, S. M.; et al. Computationally Assisted STEM and EXAFS Characterization of Tunable Rh/Au and Rh/Ag Bimetallic Nanoparticle Catalysts. *Microsc. Microanal.* **2017**, *23* (S1), 2030−2031.

(23) Li, D.; Wang, C.; Tripkovic, D.; Sun, S.; Markovic, N. M.; Stamenkovic, V. R. Surfactant Removal for Colloidal Nanoparticles from Solution Synthesis: The Effect on Catalytic Performance. *ACS Catal.* **2012**, *2* (7), 1358−1362.

(24) Blomberg, S.; Lundgren, E.; Westerström, R.; Erdogan, E.; Martin, N. M.; Mikkelsen, A.; Andersen, J. N.; Mittendorfer, F.; Gustafson, J. Structure of the Rh2O3(0001) Surface. *Surf. Sci.* **2012**, *606* (17−18), 1416−1421.

(25) Santos, M. C.; Oliveira, R. T. S.; Pereira, E. C.; Bulhões, L. O. S. Electrochemical and Mass Variation Behaviour of Rhodium Oxide Electrodes Prepared by the Polymeric Precursor Method. *Thin Solid Films* **2005**, *483* (1−2), 164−168.

(26) Yancey, D. F.; Zhang, L.; Crooks, R. M.; Henkelman, G. Au@Pt Dendrimer Encapsulated Nanoparticles as Model Electrocatalysts for Comparison of Experiment and Theory. *Chem. Sci.* **2012**, *3* (4), 1033.

DOI: 10.1021/acs.jpcc.7b10974
J. Phys. Chem. C 2018, 122, 2712−2716